Physicochem. Probl. Miner. Process., 60(3), 2024, 189758

http://www.journalssystem.com/ppmp

Physicochemical Problems of Mineral Processing

ISSN 1643-1049

Identification of tin species released in solution during water leaching of solids from the alkaline smelting (NaOH-KOH) of stanniferous ores

Phalaris Yuma M. [1], Bertin Kitungwa K. [1], Pierre Kalenga Mubiayi [2], Michel Shengo L. [1], Nosipho Moloto [2], Grace Ngubeni [2], Marsi Mbayo K. [1], Crépin Kyona W. [1]

[1] Department of Chemistry, Faculty of Sciences, University of Lubumbashi, Haut-Katanga DR Congo

[2] Faculty of Sciences, Molecular Science Institute, African Research Universities Alliance-Materials for Energy and Nanotechnology, University of Witwatersrand, Johannesburg, RSA

Corresponding authors: yumaphalaris@gmail.com (Phalaris Yuma), Kalenga.Mubiayi@wits.ac.za (Pierre Mubiayi)

Abstract: Tin species were studied from Makundju ores in DRCongo. The identification of tin species released in aqueous solution during leaching of solids from the alkaline smelting (NaOH-KOH) was done to prepare added-value mining products on tin ores mined in the eastern DR Congo. Prior to alkaline fusion to have the smelting products (SP), the initial sample (IS) was processed for tests and characterization of tin species. Alkaline fusion in molten KOH-NaOH system was used and leached solution was considered for further analyses. Various physicochemical techniques including X-ray fluorescence spectrometry (XRF), scanning electron microscopy (SEM), X-ray diffraction (XRD), thermogravimetric analysis (TGA) and FTIR spectroscopy were used to characterize the initial ore and the molten cake. Water leached cake solution at a solid/liquid ratio of 1:10 was used to identify and characterize tin species. ICP-OES analysis of the pH 11.9 solution revealed a content of 4506.3 ppm, which is equivalent to a 95.87% leaching yield. Such yield attests to the stable $Sn(OH)_{6(aq)}^{2-}$ ion as confirmed by UV-Vis. Crystallizations of $M_2Sn(OH)_{6(s)}$ (M = Na and/or K) was studied using XRD, FTIR and TGA. As pH decreases below 9, $Sn(OH)_{6\,(aq)}^{2-}$ ion changes to other tin species such as $Sn(OH)_{5\,(aq)}^{-}$, $Sn(OH)_{4\,(S)}$, $Sn(OH)_{3\,(aq)}^{+}$, $Sn(OH)_{2\,(aq)}^{2+}$, $Sn(OH)_{(aq)}^{3+}$ and $Sn_{(aq)}^{4+}$. The stability of each the tin species was determined at different pH values in aqueous solution. Hence, alkaline hexahydroxostannate nanoparticles, used in many electronic applications, can be produced from tin ores.

Keywords: tin ore, alkaline smelting, solids leaching, characterisation, tin species identification

1. Introduction

Tin and its oxides are widely used materials due to properties such as a high degree of transparency in the visible spectrum, strong physical and chemical interaction with adsorbed species, low operating temperatures, and high thermal stability in air (up to 500°C) (Armor, 1995; Bordignon, 2009).

Stannous oxide (romarchite, SnO) and stannic oxide (cassiterite, SnO_2) are the main two types of oxides as they contain tin in oxidation states of +2 and +4 repectively. SnO_2 is more stable and used in optoelectronic devices, electrodes for lithium-ion batteries, solar cells, transistors and gas sensors to detect combustible gases (Torre-Abreu et al., 1997). Cassiterite is also used in the manufacture of apparatus and pipes for the food industry, alembic lids, refrigeration apparatus, industrial tanks, welding rods, ornamental or table crockery, toys, organic pipes, etc. (Torre-Abreu et al., 1997). In ores from Makundju (DR Congo), cassiterite is the predominant mineral (Akilimali, 2016).

The metallurgical extraction of tin is difficult, due to the impurities (iron and silicon) that accompany it in various types of its ores (Grant, 2001). The extract tin, its pyrometallurgical and hydrometallurgical processes are set according to the mineral composition of the ore (Gostishchev et al., 2008 Habashi, 1997).

DOI: 10.37190/ppmp/189758

However, there are challenges associated with pyrometallurgical techniques including excessive energy consumption (Banasik, et al., 2022) and the formation of certain insoluble compounds of iron and silicon after melting at high temperatures (El Deeb et al., 2015; Zijian et al., 2017).

Nevertheless, several routes have been proposed although they could not go beyond the laboratory scale (Fecko et al., 2011; Cheng et al., 2011; Jha et al., 2012; Havilik et al., 2011). On one hand, direct leaching under severe conditions (high temperature and sometimes high pressure) has been proposed in media such as HCl and Na_2S. On the other hand, acid-soluble tin oxide was obtained after leaching with an oxidizing reagent for removal of sulfur, followed by reductive melting at 1300-1400°C (Pearson et al., 1977; Xuan., 2022).

Other researchers carried out industrial-scale smelting trials of tin ores in the temperature range of 850 -1000°C, using magnetite or the $NaCO_3$-$NaNO_3$ mixture in a CO-CO_2-rich atmosphere (Ayeni et al., 2013; El Deeb et al., 2015; Zhang et al., 2016). However, tests resulted in numerous problems such as a higher melting temperature, longer melting time and significant leakage of tin through volatilization (Yang et al., 2023).

To address issues related to the melting temperature and improve tin leaching yield, Yuma et al (2020) subjected to leaching solids from the alkaline (NaOH-KOH) smelting of a tin concentrate mined at Kalima, in the eastern DR Congo. The tin leaching yielded 96% when the smelting was conducted at 350°C for 90 minutes, with the mass ratio tin concentrate/(NaOH- KOH) set a 1:5. For this purpose, 10 g of melt was stirred for 30 minutes in 100 ml of water at room temperature.

To extract tin from leaching solution, identification and characterization of tin species present under different thermodynamic conditions need to be considered.

The present research used an aqueous leach solution of residus collected from alkaline smelting of a tin concentrate from the Makundju site (DR Congo). The identification of in species released during the leaching process was achieved by techniques such as XRF, ICP-OES, XRD, UV-Vis, FTIR, TGA and SEM-EDS analysis. These studies offered possibilities of ores conversion into tin nanoparticles that would significantly improve the optical and electrical properties of semiconductor thin films.

2. Materials and methods

2.1. Sample description

Makundju site (DRC) was used for collection of tin ores. About 15 kg of samples were collected at 5 locations of the site and mixed for good representativity. This constituted the Initial Sample (IS) from which smaller amounts were used for each study. This quantity was sufficient for all tests

For better liberation of recoverable minerals, this dry sample was ground to a particle size of 75 µm (Shengo, 2013) using a vibro-grinder coupled to a vibro-screening (Jayant Scientific ind), and then distributed according to the types of analyses and tests.

2.2. Sample analysis

2.2.1. Chemical analysis

Solid samples were analyzed by an Olympus X-ray fluorescence spectrometer (XRF) and liquids by a Spectro-Arcos Inductively Coupled Plasma Optical Emission Spectrometer (ICP-OES).

For XRF measurements, the sample should further be pulverized, homogenized and pressed into a pellet. The sample trays were placed in the autosampler so that the cards bearing the tray number faced the spectrometer.

The analytical solution was obtained after filtration of the water leach solution of ore melts with NaOH (Rochelle chemicals, 99%)-KOH (Ace,85%). Prior to sample analysis, interference corrections were established and an initial demonstration of instrument performance was documented and kept on file.

2.2.2. Mineralogical analysis

Ground and dried solids were analyzed by D2PHASER-Bruker AXS X-ray Diffractometer (XRD), Zeiss Sigma Scanning Electron Microscope coupled to an energy dispersive spectrometer (SEM-EDS), Nicolet

Apex Fourier Transform Infrared Spectrometer (FTIR) and PerkinElmer 4000 Thermogravimetric Analyzer (TGA) to identify mineral species; while filtered leach solutions were analyzed by Specord Plus UV-Vis spectrophometers for species present in ionic and complex forms.

2.3. Tin ore sample roasting and smelting

The tin ore sample was first roasted in a crucible for 3 hours at 700°C to concentrate the cassiterite and remove volatile material (Lalasari et al., 2018). The roasted sample (RS) was then subjected to smelting in presence of analytical-grade NaOH and KOH. The tin ore RS was added to equal amounts of NaOH and KOH (as flux) to prepare a mixture with a sample-flux mass ratio of 1:5 (10g RS + 25g NaOH + 25g KOH). This mixture was dried in the oven at 105°C for 3 hours; it was poured into a porcelain crucible and placed in the electric oven for melting at 350°C for 1.5 hours (Yuma et al., 2020). The smelting products (SP) were left to cool in a closed vessel at room temperature prior to chemical, mineralogical and thermogravimetric analyses.

2.4. Leaching of solids from the smelting of tin ore

10 g of SP were placed in a 500 ml beaker and leached at room temperature through stirring (300 rpm) for 60 minutes, using 100 ml water as solvent. Filtration enabled separating filtrate and residues (LR) that were washed using distilled water before drying and chemically assayed to determine the leaching yield of tin. The filtrate was subjected to chemical analysis to identify released tin species in solution as well as for pH measurements. Afterward, the filtrate pH was modified through addition of HCl or NaOH, depending on the initial value to study its effect on tin species in solution. Consequently, before and after each addition of HCl or NaOH, pH and tin species were determined using a pH meter and an inductively coupled plasma atomic emission spectrometer (ICP-OES), respectively. The leaching yield of tin was determined using the following formula:

$$LY_E(\%) = \frac{(M_{SP}.C_{SP} - M_{LR}.C_{LR})}{M_{SP}.C_{SP}}.100 \quad (1)$$

where LY_E is the leaching yield of the chemical element in percents; M_{SP} is the smelting product mass in grams, C_{Sp} the chemical element content in the smelting product in percents, M_{LR} the leaching residues mass in grams and C_{LR} the chemical element content in leaching residues in percents.

2.5. Tin species crystallization and identification

The crystallization of tin species was carried out through pH adjustment of 100 ml of the supernatant liquid (filtrate) collected from the leaching of the tin ore smelting products. Water was slowly thermally evaporated (105°C) for 72 hours (Biscans, 2020) to get crystals which were identified through chemical (XRF), mineralogical (XRD, FTIR) and thermal (TGA) analyses.

3. Results and discussion

3.1. Sample analysis results

XRF spectroscopy on the initial sample (IS) and the roasted sample (RS) yielded the results shown in Table 1. IS was characterized by elemental content, while RS was characterized by oxide content (Kaminski, 2001).

Table 1 shows that IS contains tin in large amount (Sn,69.31%). IS isassociated with impurities such as Ca, K, Fe, Si and Ti. The RS contains more SnO_2 (88.64%) than the other oxides including CaO, K_2O, Fe_3O_4, SiO_2 and TiO_2. 25.03% represented all other trace elements not listed in the table, while 1.74% represented other oxides.

A positive Loss on ignition (LOI) of 1.17% was also observed in RS.; This could be attributed to dehydration, desulfurization and decarbonation. This may also explain the non-gain in weight linked to oxidation from FeO to Fe_2O_3 (CWEA, 2017). Thus, calcite would have been the precursor of CaO after this decarbonation. SnO may undergo evaporation during the roasting process according to the observations of Lalasari et al. (2018).

Mineralogical analysis by XRD of the two samples, IS and RS, yielded the spectra shown in Fig. 1.

Table 1. Chemical elements contents (%) in investigated samples

	Unit	Sn	Nb	Ta	Ti	Fe	Mn	Ca	K	Si	S	Others	LOI
IS	%	69.31	0.08	0.03	0.2	1.04	0.06	2.39	1.57	0.25	0.04	25.03	
	Unit	**SnO_2**	**Nb_2O_5**	**Ta_2O_5**	**TiO_2**	**Fe_3O_4**	**MnO_2**	**CaO**	**K_2O**	**SiO_2**		**Others**	
RS	%	88.64	0.13	0.10	0.35	1.74	0.11	3.40	1.95	0.66		1.74	1.17

LOI: Loss on ignition

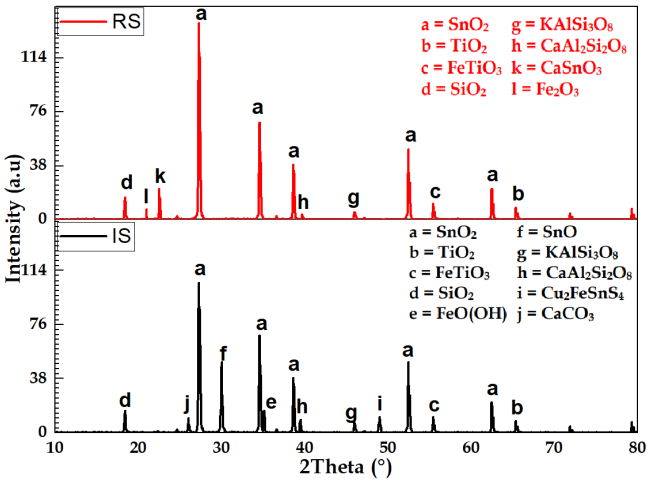

Fig. 1. XRD patterns of IS and RS samples

Spectral analysis based on the literature (Rangel et al., 2011; Floriano et al., 2014; Palanisamy et al., 2019; Clavier, 2015; Marinho et al., 2014; Janardhan et al., 2018; Buscail 2018; Namwong et al., 2010; Zhao et al., 2016; Miao et al., 2017; Thriveni et al, 2014) have revealed six (6) common minerals, namely cassiterite (a), rutile (b), ilmenite (c), quartz (d), orthoclase (g) and anorthite (h). The goethite (e), romarchite (f), stannite (i) and calcite (j) identified in IS have disappeared after roasting; whereas, in RS, two (2) new minerals have appeared, megawite (k) and hematite (l). These findings would be supported by thermogravimetric analysis, as it justifies the positive loss on fire observed in Table 1 and the decomposition reactions reported. So, both samples contain tin in the stable mineral form of cassiterite (SnO2) (Floriano et al., 2014). The roasting process allowed cassiterite to be concentrated as its peaks (a) are more intense in RS.

EDS analysis yielded the mineral distribution values recorded in Table 2 and the spectrum shown in Fig. 2(b).

Table 2. EDS mineral distribution of initial sample (IS)

Element	Ca K	K K	O K	Al K	Si K	Fe K	Ti K	Sn L	Total
Weight (%)	4.1	3.1	38.2	2.4	2.9	1.8	1.3	46.2	100
Atomic (%)	10.1	8.6	64.4	1.9	2.8	0.9	0.8	10.5	

All these elements revealed from EDS were reported in the different mineral structures observed by XRD. SEM Fig. 2(b) shows compositional and topographical contrasts throughthe difference between lightgrey, grey and black regions. Although light regions may be in the majority, some are raised from the grey background and vice versa; tin oxide regions appear as light zones (Laghrib, 2018). According to Laghrib (2018), SnO and SnO_2 grains come together to form aggregates. Cassiterite (strong white relief), anorthite (weak relief white-grey alterative face), orthoclase (different lustre of the two crystals), rutile (strong black relief), quartz (presence of several microcracks randomly distributed in the matrix) and ilmenite (opaque, black and sub-metallic lustre) could be identified. These results corroborate those of chemical analysis and XRD.

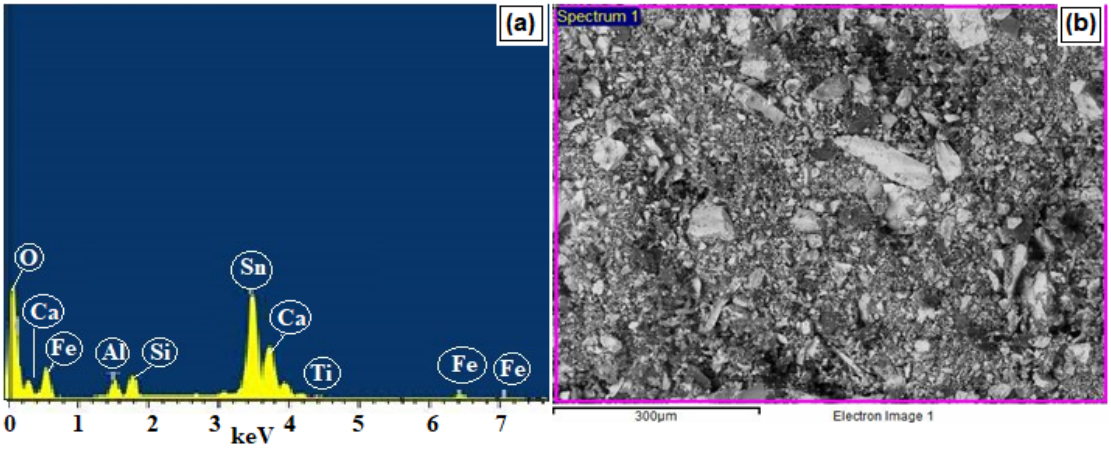

Fig. 2. (a) EDS spectrum and (b) SEM image of the initial sample (IS)

In contrast to roasting, thermogravimetric analysis was carried out in the presence of nitrogen. The TGA and DTG curves (Fig. 3) for the IS reflect those of an oxide-rich ore sample, with a weight loss of 1.29%. The DTG curve shows three endothermic decomposition bands appearing successively at 167°, 460° and 825°C. No exothermic bands were observed, i.e. there was no significant oxidation that would affect weight gain throughout these analyses. Thus, the three bands are attributed to for dehydration (167°C), decarbonation (460°C) and desulfurization (825°C) reactions (Navarro et al., 2009). These reactions are well explained from the TGA curve, which shows four ranges of low weight loss as a function of increasing temperature, from 160°-455°C (I), 455°-475° (II), 475°-818°C (III) and 818°-864°C (IV) before the curve stabilizes up to 900°C. The first interval (I) corresponds to residual water loss and dehydration of goethite (0.55%). The second (II) shows a loss of 0.14% due to calcite decarbonation. The third (III), with a loss of 0.38%, explains the first stage of Cu_2FeSnS_4 desulfurization. The last (IV) shows a loss of 0.22% due to the second desulfurization step of $FeSnS_3$ in the presence of hematite (Tabelin, et al., 2016). These four temperature ranges can be explained by the following decomposition reactions:

$$2FeO(OH)_{(s)} \rightarrow Fe_2O_{3\,(s)} + H_2O_{(s)} \quad (2)$$

$$CaCO_{3\,(s)} \rightarrow CaO_{(s)} + CO_{2\,(g)} \quad (3)$$

$$Cu_2FeSnS_{4\,(s)} \rightarrow FeSnS_{3\,(s)} + Cu_2S_{(g)} \quad (4)$$

$$FeSnS_{3\,(s)} + 8Fe_2O_{3\,(s)} \rightarrow 17FeO_{(s)} + SnO_{2\,(s)} + 3SO_{2\,(g)} \quad (5)$$

These findings are consistent with those of chemical (loss on ignition) and mineralogical (XRD) analyses.

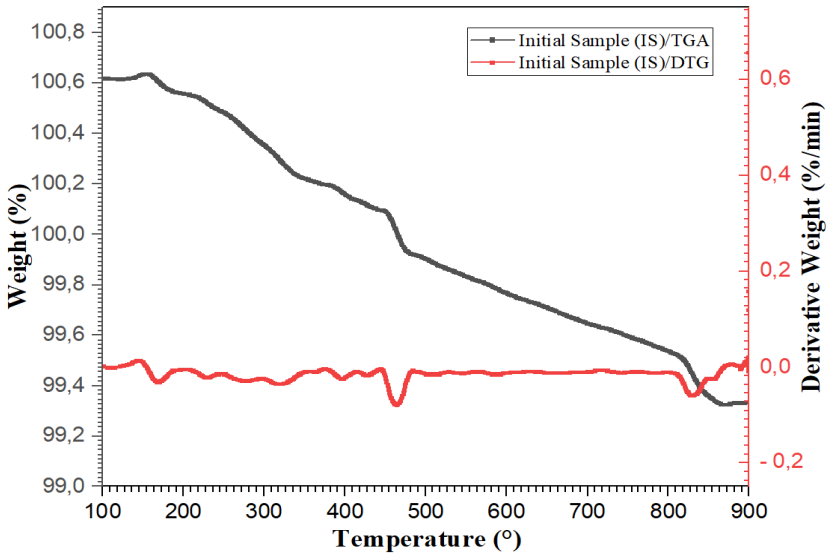

Fig. 3. TGA and DTG curves for the IS from 100 to 900°C at a heating rate of 10°C/minute

3.2. Tin ore smelting products characterization

The difference in mass between the mixture before melting and that of the molten sample was 6.6%, mainly due to the evaporation of water during the melting process. This is possible because there would be the formation of products such as M_2SnO_3, $M_2SiO_3$and also $M_8SnSi_6O_{18}$ (M= Na and/or K) reported in the literature (Bunnakkha et al, 2012; Yuma et al. 2020). Chemical analysis of RS and SP by XFR led to amounts gathered in Table 3.

Table 3. Elemental composition of RS and SP samples

Sample	Unit	Sn	Nb	Na	Ti	Fe	Mn	Ca	K	Si
SP	%	51.89	0.02	2.14	0.12	0.49	0.02	1.47	4.68	0.11
RS	%	69.82	0.09	0.08	0.21	1.26	0.07	2.43	1.62	0.31

It should be noted that, except for Na and K, all the elements present in the SP have lower contents than those in theRS. This is mainlty because the flux (NaOH+KOH) added to the RS sample increased Na and K contents while diluting those of the other elements.

Table 4 and Fig. 4 show the scanning electron microscopy-energy dispersive spectrometry (SEM-EDS) analyses of SP. Amorphous and crystalline minerals were present.

The EDS spectrum in Fig. 4(a) contains peaks of different intensities related to the presence of the main chemical elements (Table 4). These include oxygen, tin, potassium, sodium, aluminium, silicon and carbon. The presence of all these elements, except carbon, may be a result of a change in the structure of the minerals identified Fig. 2. This could then be confirmed by XRD pattern of SP sample. Fig. 4b helps visualize an amorphous structure speckled with silica grains (circled in red) and dominated by cassiterite features (framed in blue). These can be viewed as precursor of stannate, silicate and aluminosilicate, which are likely to form after the sample smelting (Bunnakkha et al, 2012). The hollow skeleton, as can be seen through images (c) and (d) of Fig. 4, suggests a microporous structure linked to the presence of the stannate group, as stated by other researchers (Wang et al., 2022; Zhang et al., 2014). Fig. 4d shows clear particle agglomeration, size distribution and a microporosity which corresponds to the presence of a molten phase made of M_2SnO_3 (with M representing Na and/or K) appearing as a smooth surface layer of M_2O species overlying an irregular surface of SnO_2.

Table 4. EDS mineral distribution of smelting products (SP)

Element	C K	O K	Na K	Al K	Si K	K K	Sn L	Total
Weight (%)	17.52	36.71	8.38	5.08	0.41	3.68	28.22	100.00
Atomic (%)	24.47	39.43	5.32	3.30	0.24	2.01	30.19	

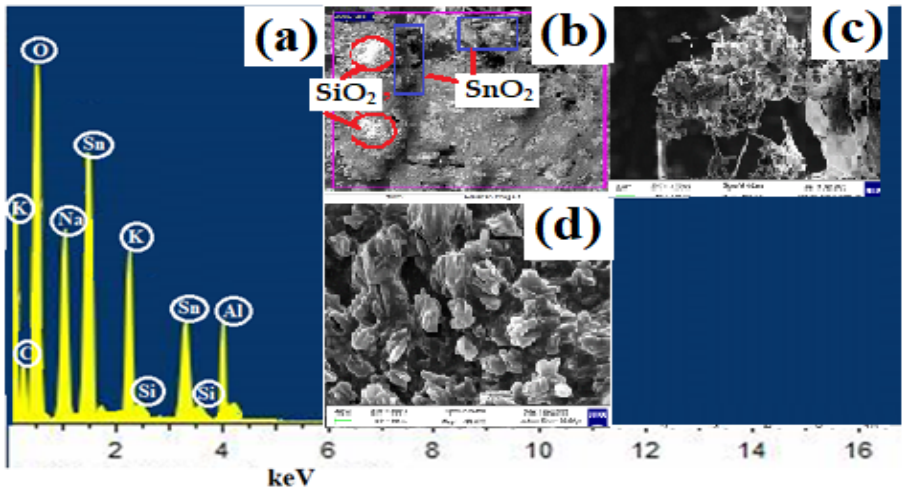

Fig. 4. EDS spectrum (a) and SEM images (b-d) of minerals in SP

The XRD analysis in Fig. 5 shows that SP relatively less crystalline than that of the RS with many reference peaks disappearing and new, less intense peaks appearing. This shows possible formation of new compounds, some in amorphous form and others in crystalline form. Based on the literature (Wang et al., 2022), the SP spectrum analysis shows the formation, after melting, of six new compounds: (1) = $M_2Sn_3O_7$, (2) = M_2SnO_3, (3) = M_4SnO_4, (4) = M_2SiO_3, (5) = M_2TiO_3 and (e) = FeO(OH), with M = Na and/or K. The first three tin compounds (1, 2 and 3) are fusion products due to endothermic reactions of SnO_2 with flux (NaOH and KOH) (Zhang et al., 2014). The other two compounds (4 and 5) are the successive products of quartz and rutile. The background noise could represent amorphous phases that formed during the melting process.

According to Baird et al. (2023), the identification of SnO_2 peaks in the SP spectrum is justified by the reaction of M_2SnO_3 formed in contact with atmospheric CO_2 during cooling of the melt products.

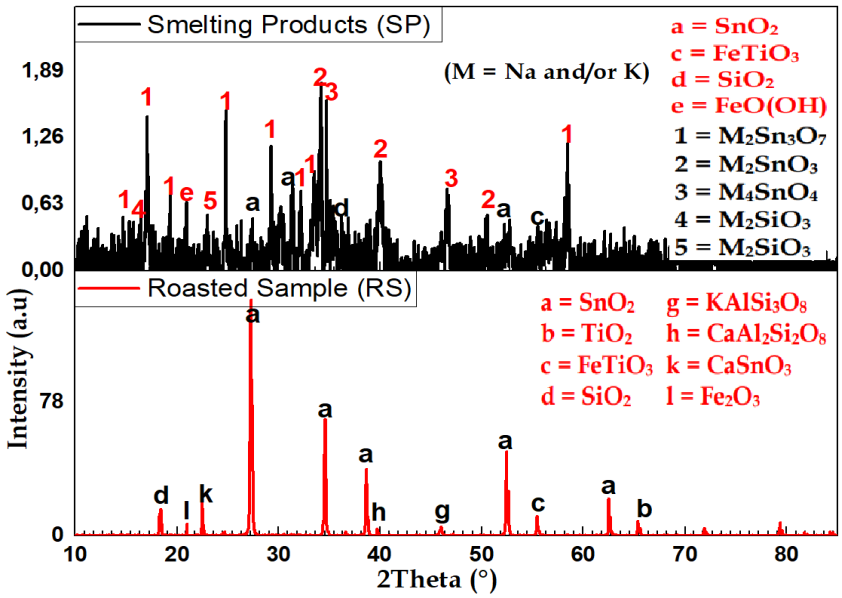

Fig. 5. XRD patterns of SP and RS samples

Reactions (6), (7), (8), (9), (10), (11), (12) and (13) explain the formation of different products (M = K or Na):

$$SnO_2 + 2MOH \rightleftharpoons M_2SnO_3 + 2H_2O \quad (6)$$

$$2SnO_2 + M_2SnO_3 \rightleftharpoons M_2Sn_3O_7 \quad (7)$$

$$M_2SnO_3 + 2MOH \rightleftharpoons M_4SnO_4 + 2H_2O \quad (8)$$

$$TiO_2 + 2MOH \rightleftharpoons M_2TiO_3 + 2H_2O \quad (9)$$

$$M_2SnO_3 + CO_2 \rightleftharpoons M_2CO_3 + SnO_2 \quad (10)$$

$$M_2SiO_3 + CO_2 \rightleftharpoons M_2CO_3 + SiO_2 \quad (11)$$

$$SiO_2 + 2MOH \rightleftharpoons M_2SiO_3 + 2H_2O \quad (12)$$

$$Fe_2O_3 + H_2O \rightleftharpoons 2FeO(OH) \quad (13)$$

The smelting product was found to be hygroscopic, attracting atmospheric water vapor as it cooled down. Thermogravimetric analyses were carried out to understand its thermal behavior as shown in Fig. 6. The TGA and DTG curves provide relevant information on certain decomposition reactions. The DTG curve shows three bands of endothermic decomposition at temperatures of 141, 397 and 865°C. Residual water caused by the smelting product during cooling was released at 141°C. The same applies to the hydroxyl groups of goethite formed (Equation 13) and unconverted KOH or NaOH, which were eliminated at 397°C. The final decomposition temperature, 865°C, is attributed to the decarbonation of M_2CO_3 produced by reactions (11) and (12) (Widmann, 2001).

TGA curve of SP reveals three significant events in terms of weight loss as a function of temperature. The first weight loss (11.4%) corresponds to the removal of water from hydration, in 52-241°C

temperature range. The second weight loss (5%) is due to maximum hydroxyl removal in 241-762°C temperature range. The third weight loss (9.8%) occurs in the temperature range of 762-997°C, due to the decomposition of M_2CO_3 to form M_2O and release CO_2. Stable oxides (Na_2O, K_2O, SnO_2, TiO_2, etc.) crystallize out completely at temperatures above 1000°C (Widmann, 2001).

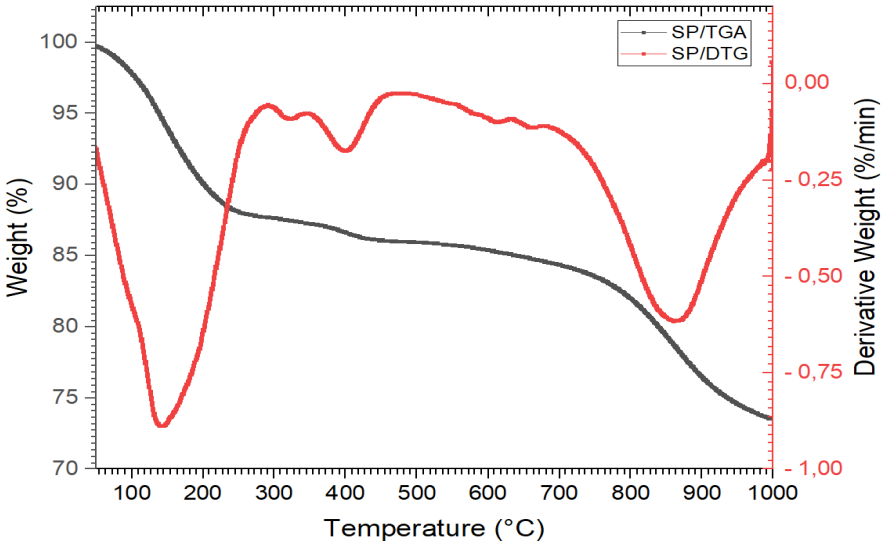

Fig. 6. TGA and DTG curves of SP in the temperature range of 50° - 1000°C, at heating rate of 10°C per minute

3.3. Characterization of the molten cake leach solution

The chemical composition of aqueous solution from the smelting products water leaching is depicted in Table 5. This solution contains tin at high concentration (4506.3 ppm). Then other elements had their concentrations decreasing in the following order: K, Na, Si, Ca, Nb, Mn, Ti and Fe.

The tin leaching yield achieved 95.87%, a value close to fthat reported by Yuma et al (2020) but higher than the ones from previous studies in literature (Bunnakkha et al 2012; Zhang et al., 2019; Zhang et al.,2014) with the use of higher temperatures. As for other chemical species released in solution, except Fe, the leaching yield was above 50%. Given that the pH was equal to 11.9, literature (Yuma et al. , 2020; Zhang et al., 2019) states that one may find chemical species such as $Sn(OH)_6^{2-}$, $Sn(OH)_5^-$, $Si(OH)_6^{2-}$, $HSiO_3^-$ and SiO_3^{2-} in the aqueous solution from the smelting products leaching, using water as solvent.

Table 5. Chemical species contents in analyzed sample and their leaching yield

Sample (Analysis method)	Units	Chemical species								
		Sn	Nb	Na	Ti	Fe	Mn	Ca	K	Si
Filtrate (ICP-OES)	ppm	4506.30	244.50	1327.90	109.30	43.20	135.30	344.10	2032.40	439.70
Leaching yield	%	95.87	55.36	97.61	93.71	19.65	31.12	54.33	98.31	92.45

Fig. 7 shows the study of species of tin released in the aqueous solution versus pH. 1M HCl (1M NaOH) solution was used to decrease (increase) pH. Tin content decreased in the pH range of 1 - 4. An increase in tin content occurred in the pH range of 5 -9. The initial content of of in the aqueous solution was achieved in the pH range of 9 -13.

The UV-Vis absorption spectra (Fig. 8) enabled identifying chemical species of tin in the aqueous solution for different pH values. The initial aqueous solution at pH 11.9 gave the light absorptions in the visible and ultraviolet regions. Tang et al (2020) reported an absorption band at 210 nm corresponds to excess NaOH that rendered alkaline the aqueous solution. The absorption band at 310 nm reveals the presence of tin species as $Na_2Sn(OH)_6$ whereas at 470 nm, tin species exist as $K_2Sn(OH)_6$ (Jiang et al., 2013; Moshtaghi et al., 2015).

The aqueous solution with the pH set at 7.5 through addition of 1M HCl solution showed five absorption bands. The band observed below 200 nm corresponds to NaCl arising due to NaOH and $Na_2Sn(OH)_6$ neutralization in presence of HCl (Tang et al. 2020). As for the remaining four absorption bands (240, 461, 569 and 648 nm), they highlight KCl formation arising due to the neutralization reaction of KOH and $K_2Sn(OH)_6$ by added HCl (Bouhdjera et al., 2012).

The aqueous solution (at pH 1) gave an absorption band below 200 nm is assigned to NaCl formation. The three bands at 250, 471 and 510 nm, respectively are attributed to other compounds as reported by Tang et al (2020). These reveal a charge transfer that arisen between Sn^{4+} and Cl^- species leading to formation of $SnCl^{3+}$, $SnCl_2^{2+}$, $SnCl_3^+$ and $SnCl_4$ complexes ($Sn^{4+} + nCl^- \rightarrow SnCl_n^{4-n}$ with $n \leq 4$). The absorption band at 471 nm may also account for the presence of KCl (Nakamoto, 2008; Samahi, 2019).

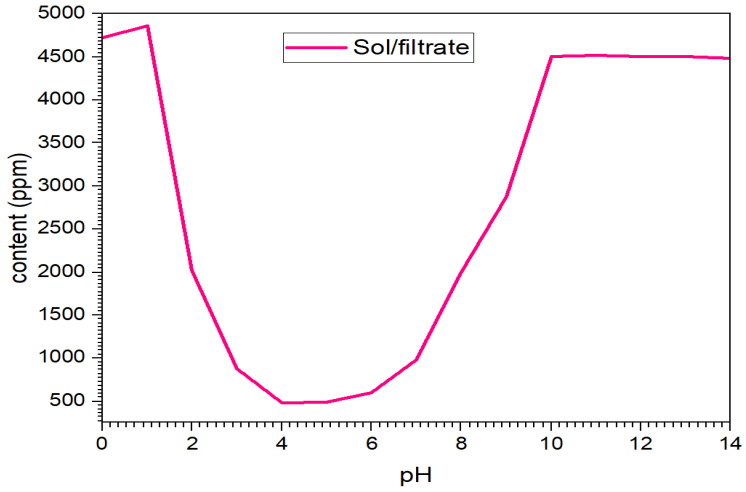

Fig. 7. Tin content versus the aqueous solution pH

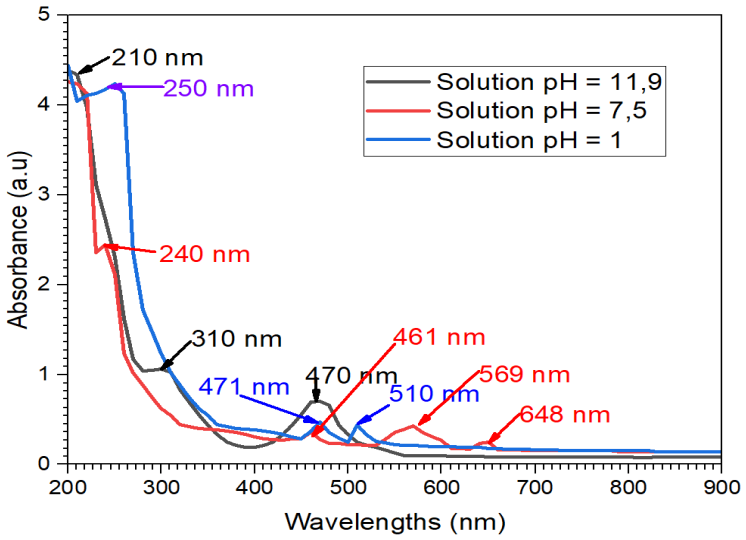

Fig. 8. UV-Vis spectra of the aqueous phase et selected pH

3.4. Characterization of crystals from solutions

To reinforce the aboveabove-mentioned findings, other analytical techniques (XRD, FTIR and TGA) were used to characterize crystals formed in solution at given pH values.

The spectra provided by XRD analysis of crystals from solutions at different pH values and the pH 7.5 precipitate are plotted in Fig. 9.

The XRD diagram of crystals prepared from aqueous solution at pH 11.9 reveals the presence of hydrated Na and/or K stannate (a), tin dioxide (b), hydrated Na and/or K silicate (c) and titanium dioxide (d). These products result from the crystallization of soluble Na and/or K hexahydroxostannate,

hexahydroxosilicate and titanate. The bump observed at the beginning of the spectrum may be due to the presence of an amorphous quartz substrate (Sladkevich et al., 2009). This also suggests that the aqueous solution of the smelting product (SP) is of low purity.

The two XRD patterns of the crystals from the pH 1 and 7.5 solutions gave the same products: sodium (s) and potassium (p) chlorides. The tin tetrachloride in the pH1 solution was not identified, as could not crystallize owing to its physical and chemical properties under the set conditions (Samahi, 2019). Under normal pressure, tin tetrachloride has a melting point of -33.5°C and a boiling point of 111°C (CHEMOS, 2022). Hence, its absence in crystals at pH 1 is justified by its evaporation during the crystallization process. However, in crystals at pH 7.5, the hexahydroxostannate ion was neutralized by HCl to yield $Sn(OH)_4$ precipitate. Neutral Na and K chlorides were also crystallized and subsequently identified by XRD.

The XRD pattern of the precipitate at pH 7.5 revealed the presence of $Sn(OH)_4$ which resulte from the neutralization of the hexahydroxostannate ion by hydrochloric acid, as reported above. The appearance of NaCl in this precipitate would be due to contamination through filtration.

These results arecorrelate with those from UV-Vis analysesand previous research (Sladkevich et al., 2009; Wu et al., 2012).

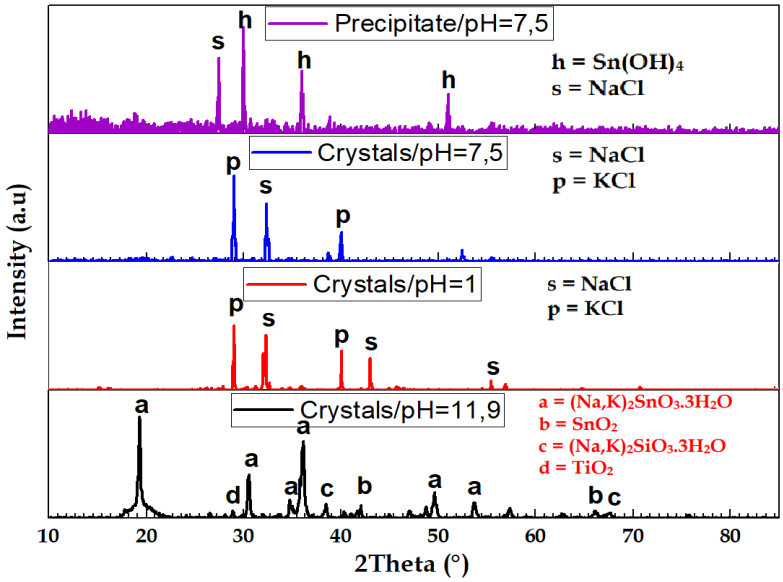

Fig. 9. XRD patterns of crystals from solutions of different pH (11.9, 1, 7.5) and precipitate at pH 7.5

Fig. 10 shows FTIR analysis of crystals formed from solutions at pH of 11.9, 7.5 and 1 and from precipitate at pH 7.5. The spectra confirmed the presence of $M_2Sn(OH)_{6\,(aq)}$ (M = Na or K) in the aqueous solution.

The FTIR spectrum of crystals that formed at pH 11.9 presents five absorption centres. The absorption band related to OH groups in hexahydroxostannate de Na and/or K and to adsorbed water appears at 3598.5 cm^{-1}. Bands that appear at 1604.5 and 1419.4 cm^{-1} correspond to the axial and anti-symmetric vibrations related to OH group in hexahydroxostannateof Na and/or K. Bands observed at 821.5 and 686.5 cm^{-1} are assigned to the metal-hydroxyl bond. As for metal-oxygen vibrations related to M-OH and M-OH-M, their absorption band can appear between 1100 and 200 cm^{-1}, depending on the mass of the metal. These findings are consistent with data from literature (Moshtaghi et al., 2015).

The FTIR spectrum of crystals that formed at pH7.5 presents two bands. According to Deshmukh et al (2012), the band at 1425.1 cm^{-1} corresponds to the adsorbed OH group whereas the one at 1095.4 cm^{-1} is associated with stretching vibrations related to Si-O-Si bonds. Indeed, according to Zerzouf (2005), tin precipitation can result in $Sn(OH)_4$(s) formation at this pH. According to Nakamoto (2008), NaCl and KCl formation in the aqueous solution is associated to absorption bands observed at wave numbers below 200 cm^{-1}.

This finding is backed by the FTIR spectrum of the precipitate that formed at pH7.5. On the latter spectrum, one observes a single band at 1108.9 cm^{-1} that related to vibrations occurring in the Sn-O-Sn

lattice of SnO_2, owing to the release of two water molecules, as dehydration products of $Sn(OH)_4$(s) or $SnO_2.2H_2O$ (s).

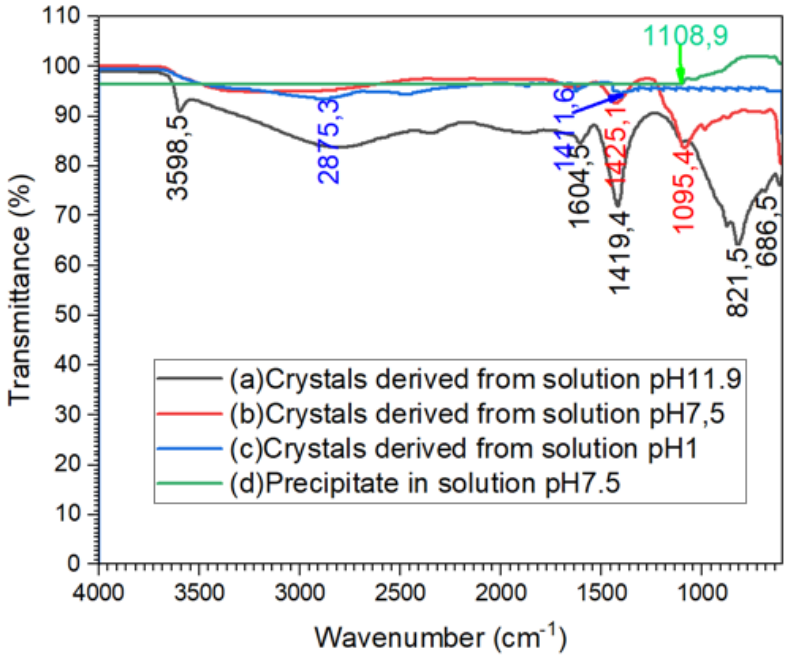

Fig. 10. FTIR spectra of crystals at pH 11.9 (a), 7.5 (b), 1 (c) and precipitate at pH 7.5 (d)

As for the FTIR of the crystals from solution at pH of 1, two bands at 2875.3 and 1411.6 cm^{-1} were observed. They are not attributed to the expected products (NaCl, KCl and $SnCl_4$). According to Nakamoto (2008), tetrahedral $SnCl_4$ (aq) is a water-soluble liquid. In the Raman spectrum, it presents four fundamental vibration modes related to absorption bands that appear in the low-frequency region. As for NaCl and KCl, they present absorption bands at 164 and 148 cm^{-1} (Nakamoto, 2008). These two bands represent those of νOH and 2δOH respectively which, indeed, were observed for the OH group of adsorbed water as 2875.3 cm^{-1} is almost double 1411.6 cm^{-1} giving the possibility of having a strong Fermi-type resonance (Deshmukh, et al., 2012; Sergent, et al., 2002).

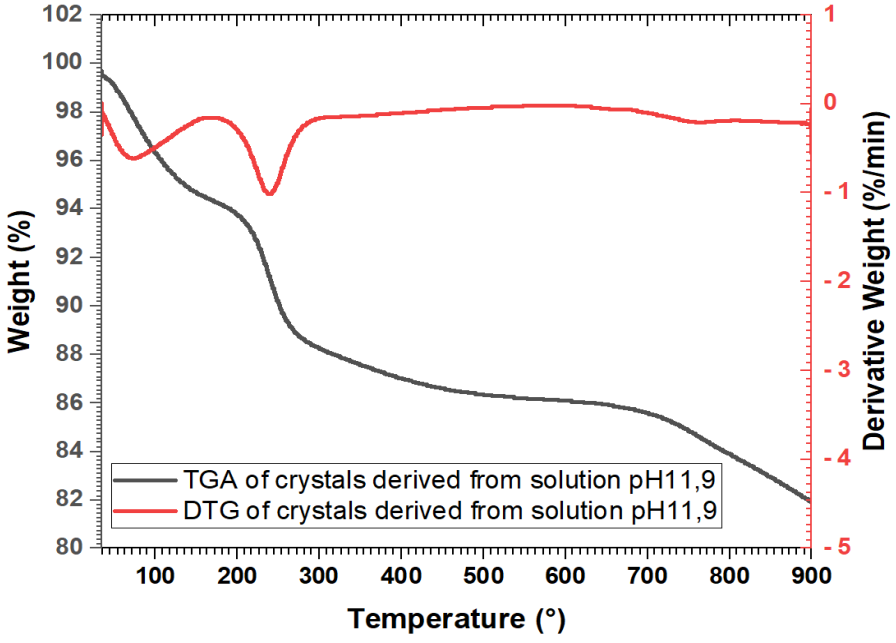

Fig. 11. TGA and DTG curves in the temperature range 35-900°C, with the heating rate of 10°C per minute, provided by crystals formed in aqueous solution at pH 11.9

The DTG curve (Fig. 11) shows two distinctive endothermic peaks at 75° and 234°C. They correspond to the respective decomposition of residual water and water associated with hexahydroxostannate and hexahydroxosilicate of Na and/or K, producing stannate and silicate of Na and/or K.

The TGA curve showed a loss of 18.1% realized in four stages between 35 and 900°C. The first two stages (38-198.7°C and 198.7-298.8°C) appear to be significant and attestthe removal of residual water and water system (Zhuang et al., 2010). The third weak slope results from the continued removal of the OH group from the hydroxides that produce the various oxides (SnO_2, SiO_2, TiO_2, Na_2O and K_2O) above 900°C.

The fourth stage justifies the decarbonation of the carbonate products formed by the reaction between atmospheric CO_2 and hydrated Na and/or K stannate during crystallization. According to Sladkevich et al (2009), the high tin content in the particles of the Na and/or K hexahydroxostannate products formed after crystallization explains the high Bronsted-Lowry alkalinity that attracts CO_2 from the atmosphere.

The above XRD, SEM, TGA, UV-Vis and FTIR analyses confirm that alkaline melting of SnO_2 or SiO_2 in the presence of NaOH-KOH gives the water-soluble compounds (M_2SnO_3 or M_2SiO_3) according to chemical equations (14) and (15):

$$M_2SnO_{3\,(s)} + 3H_2O_{(l)} \rightleftharpoons M_2Sn(OH)_{6\,(aq)} \quad (14)$$

$$M_2SiO_{3\,(s)} + 3H_2O_{(l)} \rightleftharpoons M_2Si(OH)_{6\,(aq)} \quad (15)$$

The crystallization process fromaqueous solution at different pH values, takes place as per reactions shown below while considering the physicochemical properties of the compounds formed (Zerzouf, 2005):

- Aqueous solution given by smelting products dissolution in water (pH=11.9):

$$2M^+_{(aq)} + Sn(OH)^{2-}_{6\,(aq)} \rightleftharpoons M_2SnO_3.3H_2O_{(s)} \quad (< 140°C) \quad (16)$$

$$2M^+_{(aq)} + Sn(OH)^{2-}_{6\,(aq)} \rightleftharpoons M_2SnO_{3(s)} + 3H_2O_{(g)} \quad (> 140°C) \quad 17)$$

- Aqueous solution with pH adjusted at 7.5:

$$2M^+_{(aq)} + Sn(OH)^{2-}_{6\,(aq)} + 2HCl_{(aq)} \rightleftharpoons Sn(OH)_{4\,(s)} + 2H_2O_{(g)} + 2MCl_{(s)} \quad (< 275°C) \quad (18)$$

$$Sn(OH)_{4\,(s)} \rightleftharpoons SnO_{2\,(s)} + 2H_2O_{(g)} \quad (> 275°C) \quad (19)$$

- Aqueous solution with pH adjusted at 1:

$$2M^+_{(aq)} + 2Cl^-_{(aq)} + Sn(OH)_{4\,(s)} + 4HCl_{(aq)} \rightleftharpoons SnCl_{4\,(g)} + 4H_2O_{(g)} + 2MCl_{(s)} (> 111°C) \quad (20)$$

4. Conclusions

Tin species were successfully identified and characterized in a water-leach solution of the molten cake using analytical techniques such as XRF, ICP-OES, XRD, UV-Vis, FTIR, TGA and SEM-EDS. This molten cake was prepared from the alkaline fusion of tin ore from Makundju (DR Congo) in the NaOH-KOH system, reducing the fusion temperature to 350°C. The aqueous solution was loaded with tin (4508.3 ppm), with a best tin leaching yield of 95.87%. UV-Vis spectroscopic analysis of the original solution at pH of 11.9 revealed the presence of stable $Sn(OH)^{2-}_{6\,(aq)}$ ions. XRD, FTIR and TGA analyses of products from the crystallization of tin species from the original solution allowed for identification of $Na_2Sn(OH)_6(s)$, $K_2Sn(OH)_6(s)$ and/or $KNaSn(OH)_6(s)$. Gradual addition of hydrochloric acid (HCl) to the aqueous solution reduced the pH from 11.9 to 1, with conversion of $Sn(OH)^{2-}_{6\,(aq)}$ ions successively to $Sn(OH)^{-}_{5\,(aq)}$, $Sn(OH)_{4\,(S)}$, $Sn(OH)^{+}_{3\,(aq)}$, $Sn(OH)^{2+}_{2\,(aq)}$, $Sn(OH)^{3+}_{(aq)}$ and $Sn^{4+}_{(aq)}$. Hence, tin concentrate can be used to produce $Na_2Sn(OH)_6(s)$ or $K_2Sn(OH)_6(s)$ nanoparticles with potential for future optoelectronic and photoelectric applications. A solution purification study could be envisaged to obtain tin nanoparticles of high purity.

Acknowledgments

The authors are grateful to the VLIR-UOS/Belgium Program for bearing the cost of analyses carried out for this study; they would also like to thank the University of Witwatersrand (Wits) in Johannesburg

(RSA) for accepting a team to carry out these analyses in its School of Chemistry/Faculty of Science laboratories.

References

AKILIMALI, S.M. 2016. *Gitologie, métallogénie et exploitation minière artisanale dans le Kivu: Bref aperçu sur les gisements stannifères*. Article. Le Cahier du BEGE-RDC , Journal pour la promotion des géosciences. Vol. 1, 2, pp. 26-33. 2518-4539 (En ligne), 2518-4520 (Imprimée).

ARMOR, J. 1995. *Catalytic removal of nitrogen oxides: where are the opportunities?*Art., 26(2), 99-105. (E. ScienceDirect, Éd.) Catalysis Today.

AYENI, F., ALABI, O., OKARA, R. 2013. *The Effects of Blends of Enugu Coal and Anthracite on Tin Smelting Using Nigerian Dogo Na Hauwa Cassiterite*. Article, 343-346. Journal of Minerals and Materials Characterization and Engineering.

BAIRD, R., CHANG, R., CHEUNG, O., SANNA , A. 2023. *High Temperature CO_2 Capture Performance and Kinetic Analysis of Novel Potassium Stannate*. Article, *24(2321)*, 1-23. (A. Taubert, Éd.) Int. J. Mol.Sci. MDPI.

BANASIK, L., MISKIEWICZ, R., CHOLEWA-DOMANAGIC, A., JANIK, K., KOZLOWSKI, S. (2022). *Development of tin metallurgy in Rwanda*. Article, 1-7. Metal 2022, Brno, Czech Republic, EU.

BISCANS, B. 2020. *Cristallisation en solution - Procédés et types d'appareils*. Base de données, veille technologique, documentation et expertise technique. Toulouse/France : Techniques de l'Ingénieur.

BORDIGNON, M. 2009. *Limites d'utilisation des revêtements d'étain en connectique automobile*. Archive ouverte pluridisciplinaire HAL Open Sciences, *NNT : 2009ENMP1667*. Paris: Mécanique [physics.med-ph]. École Nationale Supérieure des Mines de Paris. Récupéré sur https://pastel.hal.science/tel-00460544

BOUHDJERA, I., ADDALAA, S., CHALAB, A., HALIMIA, O., BOUDINEA, B., SEBAISA, M., & KARAA, S. 2012. *Structural and optical properties of CdSe doped KCl single crystal*. Art., 2(1), 34-37. (O. U. Co., Éd.) Journal of New Technology and Materials.

BUNNAKKHA, C., JARUPISITTHORN, C. 2012. *Extraction of Tin from Hardhead by Oxidation and Fusion with Sodium Hydroxide*. *22(01)*, 1-6. Journal of Metals, Materials and Minerals.

BUSCAIL, H. 2018. *L'analyse chimique des roches au service de la géologie*. Archive ouverte pluridisciplinaire HAL, 83p. Le Puy en Velay, France: Editions universitaires européenne, Université Clermont Auvergne - LVEEM – IUT.

CHEMOS, 2022. *Tétrachlorure d'étain. Fiche des données et de sécurité*. Article. CHEMOS. GHS 4.0- A0008518. France. Pp. 1-11

CHENG, C., YANG, F., ZHAO, J., WANG, I., LI, X. 2011. *Leaching of heavy metal elements in solder alloys*. *53*, 1738–1747. Corrosion Science.

CLAVIER, D. 2015. *Croissance hydrothermale de monocristaux isotypes du quartz-a, étude des propriétés physiques et recherche de nouvelles solutions solides avec des oxydes du bloc p (Ge, Sn) et du bloc d (Mn, V, Ti)*. Thèse de doctorat, 1-263. Montpellier, France: Université de Montpellier, Cristallographie. CWEA. 2017. *Détermination de la perte au feu des déchets, boues et des sédiments*. Rapport. Wallonie: Institut Scientifique de Service Public, Métrologie environnementale, Recherche-Analyses, Essais-Expertises.

DESHMUKH, P., PESHWE, D., PATHAK, S. 2012. *FTIR and TGA analysis in relation with the % crystallinity of the SiO2 obtained by burning rice husk at various temperatures*. *Art., 585*, 75-81. Advanced Materials Research.

EL DEEB, A., MORSI, I., ATLAM, A., OMAR, A., FATHY, W. 2015. *Pyrometallurgical Extraction of Tin Metal from the Egyptian Cassiterite Concentrate*. *6*. Egypte: IJSER.

FECKO, P., JANKOVA, I., PERTILE, E., KULOVA, E. 2011. *Bacterial leaching of Pb – Metallurgical wastes*, Metalurgija 50. *1*, 33-36. Metalurgija 50.

FLORIANO, E., SCALVI, L., SAEKI, M., SAMBRANO, J. 2014. *Preparation of TiO_2/SnO_2 Thin Films by Sol−Gel Method and Periodic B3LYP Simulations*. Article, A-I. The Journal of Physical Chemistry, American Chemical Society.

GOSTISHCHEV, V., RI, E., DOROFEEV, S., KOMKOV, V., KHOSEN, R. 2008. *RF Patent 2333268*.

GRANT, R. 2001. *Tin production in Encyclopedia of materials*. 9354-9357. (S. Direct, Éd.) Elsevier.

HABASHI, F. 1997. *Handbook of Extractive Metallurgy*. *2*, 683 - 714. New York: WILEY-VCH. doi:ISBN 3-527-28792-2

HAVILIK, T., ORAC, D., PETRANIKOVA, M., MISKUFOVA, A. 2011. *Hydrometallurgical treatment of used printed circuit boards after*. 1542–1546. Waste Management 31.

JANARDHAN, E., MAHESHWAR, M., VENKAT, P., JAIPAL, M. 2018. *Synthesis of SnO Nanopatricles – A Hydrothermal Approach*. Article, *8*, 33-37. World Journal of Nano Science and Engineering, Scientific Research Publishing.

JHA, M., KUMARI, A., CHOUBEY, P., LEE, J., KUMAR, V., JEONG, J. 2012. *Leaching of lead from solder material of waste printed circuit boards (PCBs)*. 28–34. Hydrometallurgy 121-124.

JIANG, Y., JIANG, N., LIANG, K., YUAN, C., FANG, X., XU, A. 2013. *A simple and general route to prepare functional mesoporous double-metal oxy(hydroxide)*. *Art., 1(3)*, 1-8. (R. S. Chemistry, Éd.) Journal of Materials Chemistry A.

KAMINSKI, E. 2001. *Comment connaître la teneur en masse d'un élément si l'on ne connaît que la teneur en masse de son oxyde?* Ressources scientifiques pour l'enseignement es sciences de la Terre et de l'Univers. Paris : Eduscol, Planet-Terre

KIKOUAMA, J., KONAN, K., KATTY, A., BONNET, J., BALDE, L., YAGOUBI, N. 2009. *Physicochemical characterization of edible clays and release of trace elements*. Art., 43, 135–141. (ScienceDirect, Elsevier, Éd.) Applied Clay Science. doi:10.1016/j.clay.2008.07.031

KODAMA, R., TERADA, Y., NAKAI, I., KOMABA, S., KUMAGAI, N. 2006. *Electrochemical and In Situ XAFS-XRD Investigation of Nb2O5 for Rechargeable Lithium Batteries*. Article, *153(3)*, A583-A588. Journal of The Electrochemical Society.

LAGHRIB , S. 2018. *Synthèse des films minces de : SnO2, SnO2: In par deux procédés physique et chimique et étude de leur caractérisation*. Thèse de Doctorat, 139p. Setif, Algérie: Université ABBAS- SETIF, Faculté des Sciences de l'Ingénieur, Département de Génie des Procédés .

LALASARI, L., ANDRIYAH, L., ARINI, T., FIRDIYONO, F. 2018. *The effect of temperature and addition of reducing agent on sodium stannate preparation from cassiterite by the alkaline roasting process*. Art., 020022, 1-9. (P. o. 2017), Éd. AIP Conference Proceedings 1945.

LI, Q., ZHANG, H., CHENG, B., ZOU, B., & CUI, T. 2014. *Pressure-induced amorphization in orthorhombic Ta2O5: An intrinsic character of crystal*. Article, *115(193512)*, 1-4. Journal of Applied Physics.

MARINHO, J., MONTES, R., DE MOURA, A., LONGO, E., VARELA, J., MUNOZ, R., LIMA, R. 2014. *Rapid preparation of a-FeOOH and a-Fe2O3 nanostructures by microwave heating and their application in electrochemical sensors*. Article, *49*, 572–576. Materials Research Bulletin, Elsevier.

MIAO, X., CHEN, R., & CHENG, W. 2017. *Synthesis and Characterization of Cu_2FeSnS_4 Thin Films Prepared by Electrochemical Deposition*. Article, 1-8. Materials Letters. doi:http://dx.doi.org/10.1016/j.matlet.2017.01.099

MOSHTAGHI, S., ZINATLOO-AJABSHIR, S., SALAVATI-NIASARI, M. 2015. *Nanocrystalline barium stannate: facile morphology-controlled preparation, characterization and investigation of optical and photocatalytic properties*. Art., 1-9. New York: J Mater Sci: Mater Electron.

NAKAMOTO, K. (2008). *Infrared and Raman Spectra of Inorganic and Coordination Compounds*. Volume 0. Theory of Normal Vibrations. 10.1002/9780470405840(), 1–147.

NAMWONG, P., LAORODPHAN, N., THIEMSORN, W., JAIMASITH, M., WANNAKON , A., CHAIRUANGSRI, T. 2010. *A Barium-Calcium Silicate Glass for Use as Seals in Planar SOFCs*. Article, *37(2)*,: 231-242. Chiang Mai J. Sci., j

NAVARRO, C., AGUDO, E., LUQUE, A., NAVARRO, A., HUERTAS, A. 2009. Thermal decomposition of calcite: Mechanisms of formation and textural evolution of CaO nanocrystals. *Article, 94(1)*, 578–593. American Mineralogist.

PALANISAMY, S., SRINIVASAN, S., PRABHAKARAN, A., RAJENDHRAN, N., SUBRAMANI, K., MURUGAN, V., VENKATACHALAM, R. 2019. *Infuence of nanofower FeTiO3 in carbon dioxide reduction*. Artile, *1(1230)*, 1-10. Switzerland: SN Applied Sciences, Springer Nature Switzerland AG. PEARSON, D., HOLD, G., WINTER, D. 1977. *Développement d'un procédé hydrométallurgique pour l'extraction d'étain de concentrés pauvres : 1-préparation d'une phase vitreuse lixiviable*. Transactions C (GB) 86(9). London: Institution of Mining and Metallurgy.

RANGEL, J., SANTOS, H., OLIVEIRA, M., LONGO, E. 2011. *Sintese e caracterização estrutural de SnO2 dopado com Ni. 4, 112-127*. Holos, Brésil: Instituto Federal de Educação, Ciência e Tecnologia do Rio Grande do Norte. Récupéré sur http://www.redalyc.org/articulo.oa?id=481549217008

SAMAHI, H. 2019. *Synthèse et caractérisation des complexes bases de Schiff d'étain et du nickel*. Msc. Biskra: Université Mohamed Khider de Biskra, Fac. Sc. et Techn.

SERGENT, N., GELIN, P., PERIER-CAMBYA, L., PRALIAUD, H., THOMAS, G. 2002. *Preparation and characterisation of high surface area stannic oxides: structural, textural and semiconducting properties*. Article, 54, 176–188. (Elsevier, Éd.) Sensors and Actuators B.

SLADKEVICH, S., GUTKIN, V., LEV, O., LEGUROVA, E., KHABIBULIN, D., FEDOTOV, M., PRIKHODCHENKO, P. 2009. *Hydrogen peroxide induced formation of peroxystannate nanoparticles*. Art., *50*, 229-240. (Springer, Éd.) J Sol-Gel Sci Technol.

SURESH, K., SURENDHIRAN, S., MANOJ KUMAR, P., RANJTH KUMAR, E., SYED KHADAR, Y., BALAMURUGAN, A. 2020. *Green synthesis of SnO_2 nanoparticles using Delonix elata leaf extract: Evaluation of its structural, optical, morphological and photocatalytic properties*. Research Article, 2(1735). SN Applied Sciences.

TABELIN, C., VEERAWATTANANUN, S., ITO, M., IGARASHI, T. 2016. *Pyrite oxidation in the presence of hematite and alumina: I. Batch leaching experiments and kinetic modeling calculations*. Article. Science of the Total Environment.

TANG, X., TONG, A., ZHANG, F., WANG, B. 2020. *Quantitative Analysis of NaCl, NaOH, and β-phenylethylamine in Water using Ultraviolet Spectroscopy coupled with Partial Least Squares and Net Analyte*. Article, 49(8), pp1773-1785. Sains Malaysiana.

TORRE-ABREU, C., RIBEIRO, M., HENRIQUES, C., RIBEIRO, F. 1997. *Influence of cocation on catalytic activity of CuMOR catalysts for NO SCR by propene. Effect of water presence. Art., 43*, 25-29. Catalysis Letters.

THRIVENI, T., NAM, S., & AHN, J. 2014. *Enhancement of arsenic removal efficiency from mining waste water by accelerated carbonation*. Article, 1-7. Santiago: IMPC.

WANG, J., WANG, J., GUO, X., YANG, H. 2022. *Construction of Macroporous Co_2SnO_4 with Hollow Skeletons as Anodes for Lithium-Ion Batteries*. Art., 8(257). Gels.

WIDMANN, G. 2001. *Conseils TA: Interprétation des courbes de TGA.13*, 1-20. (M. TOLEDO, Éd.) Schwerzenbach, Switzerland: UserCom 1.

WU, X., LV, G., HU, X., TANG, Y. 2012. *A Two-StepMethod to Synthesize $BaSn(OH)_6$ Crystalline Nanorods and Their Thermal Decomposition to Barium Stannate*. Art., 2012, 1-6. (T. Zhu, Éd.) Journal of Nanomaterials.

XUAN., W. 2022. *Développement d'un procédé hydrométallurgique pour le recyclage des électrodes positives de type NMC contenues dans les batteries lithium-ion usagées*. Archive ouverte pluridisciplinaire HAL open Sciences, NT : 2022LORR0074. Lorraine, France: Génie chimique. Université de Lorraine. Récupéré sur https://hal.univ-lorraine.fr/tel-03796693v2

YANG, D., WU, Z., REN, K., DONG, P., ZHANG, D., YANG, B., LIANG, F. 2023. *RecentAdvances of the ThermodynamicBehavior of Tin Species in Aqueous Solution*. 59(00). Journal of Mining and Metallurgy. Section B Metallurgy 59(00), 1-1.

YUMA, P., KITUNGWA, B., KATEULE, C., KYONA, C., WAKENGE, I. 2020. *Hydrometallurgical extraction of tin from cassiterite ore in Kalima (DR Congo) by alkaline fusion with eutectic mixture of alkali hydroxides (sodium and potassium)*. Art., 13(5), 60-67. (IOSR, Éd.) IOSR Journal of Applied Chemistry (IOSR-JAC).

ZERZOUF, O. 2005. *Contribution à la synthèse des monocristaux d'hexahydroxostannate de métaux bivalents et détermination de leurs structures cristallographiques. Thèse*, 119p. Osnabrueck: l'université Osnabrueck, Dpt Biologie/Chimie.

ZHANG, R., HE, Y., XU, L. 2014. *Controllable Synthesis of Hierarchical $ZnSn(OH)_6$ and Zn_2SnO_4 Hollow Nanospheres and Their Applications as Anodes for Lithium Ion Batteries. Art., 2(5)*, 17979–17985. J. Mater. Chem. A.

ZHANG, Y., HAN, B., SU, Z., CHEN, X., LIU, S., LIU, J., JIANG, T. 2019. *Effect of quartz on the preparation of sodium stannate from cassiterite concentrates by soda roasting process*. Art., 1-13. (MDPI, Éd.) Minerals.

ZHANG, Y., YOULIAN, Z., LIU, B. 2016. *Reduction behavior of SnO_2 in the tin-bearing iron concentrates under $CO–CO_2$ atmosphere. Part I: Effect of magnetite*. Article, 251-259. Powder Technology.

ZHAO, H., SHI, M., ZOU, J., YANG, B., LI, Y., WANG, Z., CHANG, C. 2016. *Synthesis and luminescent properties of a new cyan afterglow phosphor CaSnO3: Gd3+*. Article, 1-5. Ceramics International, Elsevier. doi:

ZHUANG, G., JIN, Y., ZHAO, H., KONG, X., LONG, L., HUANG , R., ZHENG, L. 2010. *A nanosized Gd_6Ni_3 cluster-based heterometallic coordination polymer*. Art., 39, 5077–5079. (T. R. Chemistry, Éd.) Dalton Transactions.

ZIJIAN, S., ZHANG, Y., LIU, B., CHEN, Y., LI, G., JIANG, T. 2017. *Formation mechanisms of $Fe_{3-x}Sn_xO_4$ by a chemical vapor transport (CVT) process*. (C. S. School of Minerals Processing and Bioengineering, Éd.) Changsha, China: Scientific Reports.